Int. J. Heat Mass Transfer. Vol. 35, No. 10, pp. 2335–2346, 1992
Printed in Great Britain

0017–9310/92 $5.00 + 0.00

Effect of anisotropic permeability on the transport process during solidification of a binary mixture

HOSEON YOO and R. VISKANTA
Heat Transfer Laboratory, School of Mechanical Engineering, Purdue University, West Lafayette, IN 47907, U.S.A.

(*Received* 8 *July* 1991 *and in final form* 8 *November* 1991)

Abstract—Solidification of a binary mixture (NH_4Cl–H_2O) contained in a square cavity is simulated numerically. The anisotropic permeability of the mushy region is incorporated in the model by means of a specific permeability tensor and the principal permeability ratio R. Comparison of representative results with previously reported experimental data shows that the model is capable of resolving fundamental characteristics of the solidification process. Effects of the anisotropy appear to be significant. A small permeability ratio R not only promotes the growth of the secondary layer but also results in a large concentration difference between the mushy and the pure liquid regions. Due to the liquidus temperature depression by higher concentration and the earlier developed thermal convection in the upper layer, severe remelting is also found to occur. In addition, flow interaction across the macroscopic solidification front becomes stronger with increasing permeability ratio R.

INTRODUCTION

SOLIDIFICATION of non-eutectic binary or multi-component mixtures, in contrast to pure substances and eutectic mixtures, can be characterized by the presence of a two-phase (mushy) region over an extended temperature range and a difference in solubility between liquid and solid phases. The mushy region has a microstructure similar to that of a saturated porous medium so that not only is fluid flow taking place in the region, but the flow may also interact with that of the neighboring pure liquid region. The different solubility of the species in the mushy region results in the development of concentration gradients, hence, natural convective motion can be induced by both solutal and thermal buoyancy forces in the melt pool as well as in the mushy region. The importance of double-diffusive or thermosolutal convection during solidification of binary mixtures has been well recognized in a variety of solidification processes [1–3]. It can significantly affect heat and mass transfer along the solidification front and thereby alter the solidification characteristics. Development of a more realistic mathematical–numerical model for this fundamental transport phenomenon must, therefore, be based on the experimental observations in order to obtain improved predictions of the solidification processes.

In general, the mushy region which is formed during solidification of non-eutectic mixtures under moderate cooling rates has a columnar–dendritic morphology, except during the very early and the final stage of the process. Due to the directional nature of columnar dendrites, interdendritic fluid flow depends on flow direction. When Darcy's law is adopted to describe the flow through the mushy region in macroscopic models, this directional dependence can be expressed in terms of the anisotropic permeability. In fact, there has been a number of experimental studies which have demonstrated the anisotropy of the permeability. Okamoto and co-workers [4, 5] measured the permeability of columnar–dendritic structure using a borneol–paraffin organic binary system and found that permeabilities for flow parallel and normal to the dendrites were significantly different. They also presented a functional relation of the permeability in terms of the liquid volume fraction and dendrite arm spacings. The same trends have been reported for a metal alloy system (Pb–Sn) by Nassar-Rafi *et al.* [6], who concluded that the permeability is, in fact, anisotropic in columnar–dendritic structures. Poirier [7] confirmed this fact through reexamination of the earlier experimental data.

Recently, considerable research attention has been focused on the development of sophisticated theoretical models to predict transport phenomena such as double-diffusive convection heat and mass transfer which accompany the solidification of mixtures. This is not only because there is interest in understanding solidification process, but also because the complicated transient phenomena are difficult to observe experimentally and measure with a reasonable accuracy. Comparisons of predictions based on models in some simplified geometries [8, 9] with experimental results using metal alloy analogs have been encouraging, but they have failed to achieve close quantitative agreement. The discrepancy may be attributed to many factors. For one, the anisotropy of the mushy

NOMENCLATURE

$\mathbf{B}$	body force vector
c_p	specific heat
C	concentration
Δc_p	$c_{pl}-c_{ps}$
D	mass diffusion coefficient
f	mass fraction or function
g	volume fraction or gravitational acceleration
h	enthalpy
$\mathbf{i}, \mathbf{j}$	x-, y-direction unit vectors
k	thermal conductivity
k_p	equilibrium partition coefficient
K	mean permeability
K_0	permeability coefficient
K_ξ, K_η	principal permeability components
$\mathbf{K}^{(2)}$	permeability tensor
L	latent heat or cavity length
p	pressure
R	principal permeability ratio
t	time
T	temperature
u, v	x-, y-direction velocity components
$\mathbf{V}$	velocity vector
x, y	coordinate axes.

Greek symbols

β_C	solutal expansion coefficient
β_T	thermal expansion coefficient
ξ, η	principal directions
μ	dynamic viscosity
ρ	density
ϕ	mixture quantity.

Subscripts

e	eutectic
in	initial state
l	liquid
ref	reference state
s	solid.

region should be accounted for [10]. Since the permeability is responsible for the interdendritic fluid flow and thereby affects heat and mass transfer over the entire domain, its anisotropy, as discussed before, can alter the transport processes significantly. Accordingly, the anisotropy needs to be taken into account to obtain improved predictions and to determine its effects on the transport processes as well as to establish if it can be neglected. There have, however, been no attempts to account for the anisotropy of the permeability in model predictions. The present study is motivated by this fact and is aimed to show numerically how the anisotropic permeability affects the transport process during solidification of binary mixtures.

The aqueous ammonium chloride solution (NH_4Cl–H_2O) has been chosen as the model of a binary system, because its solidification microstructure is similar to that of metal alloys which are of practical interest, and its thermophysical properties are well established [11]. Furthermore, the buoyancy factor of water-rich NH_4Cl–H_2O system is approximately -1.4, i.e. thermal and solutal buoyancy forces are of nearly the same order of magnitude, but act in opposite directions, so that this system is convenient to examine a typical pattern of double-diffusive convection. Since the focus of this study lies in investigating the effects of anisotropic permeability, a well known as well as simplified physical model has been adopted. The geometry is a two-dimensional square cavity with heating/cooling vertical walls and adiabatic horizontal connecting walls. In the numerical computations, a permeability model is constructed to accommodate the anisotropy in the governing equations. The principal permeability ratio, R, is also introduced as a measure of the anisotropy, and the simulated results are presented in terms of this parameter.

ANALYSIS

Mathematical model

Since the earlier pioneering works [11, 12] which took into account natural convection when modeling the solidification process in binary systems, various mathematical–numerical models capable of dealing with coupled fluid flow and heat and mass transfer have been proposed. A comprehensive review of the studies is available [2] in which basic features of each model are summarized. In fact, most of the formulations belong to either the continuum or the (local) volume-averaging models according to the manner in which multi-phase systems are described. Although the approaches differ from each other regarding formulation of the model equations, there is no substantial difference in the final equations which have been deduced for each model as far as the macroscopic formulation is concerned. Both of the models consist of conservation equations for total mass, momentum, energy, and species, and the supplementary thermodynamic relations for closure in similar forms. A set of equations adopted in this study can, therefore, be derived from either the continuum or the volume-averaging models. Detailed derivation of macroscopic transport equations can be found in the literature [13–16], except for the permeability in the momentum equation. The governing equations in the general forms are as follows:

$$\frac{\partial \rho}{\partial t} + \nabla \cdot (\rho \mathbf{V}) = 0 \tag{1}$$

$$\frac{\partial (\rho \mathbf{V})}{\partial t} + \nabla \cdot (\rho \mathbf{V}\mathbf{V}) = -\nabla p + \nabla \cdot (\bar{\mu} \nabla \mathbf{V}) + \rho \mathbf{B} - \frac{\bar{\mu} \mathbf{V}}{\mathbf{K}^{(2)}} \tag{2}$$

$$\frac{\partial (\rho h)}{\partial t} + \nabla \cdot (\rho \mathbf{V} h) = \nabla \cdot (k \nabla T) - \nabla \cdot \rho (h_l - h) \mathbf{V} \tag{3}$$

$$\frac{\partial (\rho \mathbf{C})}{\partial t} + \nabla \cdot (\rho \mathbf{V}\mathbf{C}) = \nabla \cdot (\rho D \nabla C_l) - \nabla \cdot \rho (C_l - C) \mathbf{V} \tag{4}$$

where mixture quantities are defined by

$$\phi = f_s \phi_s + f_l \phi_l \quad (\phi = \mathbf{V}, h, C) \tag{5}$$

and

$$\rho = g_s \rho_s + g_l \rho_l \tag{6}$$

$$k = g_s k_s + g_l k_l \tag{7}$$

$$\bar{\mu} = \rho_l \mu_l / \rho \tag{8}$$

$$D = f_l D_l. \tag{9}$$

In deriving the equations, it is assumed that the solid is stationary ($\mathbf{V}_s = 0$) and has continuous, non-deforming microstructure. The other basic assumptions involved are: (i) two-dimensional laminar flow, (ii) incompressible Newtonian fluid, (iii) local thermodynamic equilibrium, i.e. $T = T_s = T_l$ and $C_s = k_p C_l$ (for non-eutectic concentration), (iv) negligible macroscopic mass diffusion in the solid phase ($D_s = 0$), (v) negligible thermocapillary effects, (vi) negligible effects of small disturbances (e.g. dispersion fluxes, subcooling of the liquid, etc.) in the fields. If we invoke the Boussinesq approximation, the body force in equation (2) can be expressed as

$$\rho \mathbf{B} = \rho_l \mathbf{g} \mathbf{j} [\beta_T (T - T_{ref}) + \beta_C (C_l - C_{l,ref})] \tag{10}$$

where T_{ref} and $C_{l,ref}$ denote reference temperature and liquid concentration, respectively.

Here, it should be mentioned that the transport equations written on the macroscopic scale are used to resolve the two-phase as well as the single-phase regions. In typical applications, physical systems to be analyzed with a limited number of computational cells (or control volumes) encompass a large difference in scales. The solid–liquid morphology on the microscopic scale is, however, nearly fixed, being of the order of 10^{-5}–10^{-4} m, and it is important to recognize the scale effect in modeling solidification of mixtures. For this reason, the non-dimensionalization of the transport equations is less meaningful than in single-phase problems.

Since the energy equation contains temperature as well as enthalpy explicitly, it is necessary to define the enthalpy in terms of the temperature. With use of this definition, equation (3) can be reduced to the standard form of the conservation equation which is easy to solve numerically. The definition is also relevant to the thermodynamic relation of phase equilibrium from which the solid–liquid mass fraction is determined. Two concepts of the enthalpy definition have been proposed, one by Bennon and Incropera [17] and the other by Prakash and Voller [18]. The major difference between them is the selection of a dependent variable for the energy equation. In the former, the dependent variable is the total mixture enthalpy. In this case, the (equilibrium) temperature should be determined by the phase equilibrium diagram, because there is no direct relationship between the total mixture enthalpy and the temperature. If both of them are known, the mass fraction is readily calculated by combining the definitions of total phase enthalpies and the mixture enthalpy. The latter takes sensible mixture enthalpy as the dependent variable so that the temperature is directly proportional to it. Then, the mass fraction should be determined from the phase equilibrium condition. Physically, there is no fundamental difference between the two methods. The specific form of the energy equation written by either of them has the diffusion-like and/or convection-like source terms which are, however, tricky to discretize and may cause numerical difficulties. This problem can be avoided by introducing a different definition of enthalpy. A sensible enthalpy, h, is defined as

$$h = c_{pl} T \tag{11}$$

where the phase specific heats are assumed to be temperature and composition independent. With this definition and use of equation (5), the energy equation can be expressed, after some manipulation, as

$$\frac{\partial (\rho h)}{\partial t} + \nabla \cdot (\rho \mathbf{V} h) = \nabla \left(\frac{k}{c_{pl}} \nabla h \right) + \frac{\Delta c_p}{c_{pl}} \frac{\partial}{\partial t} (f_s \rho h) + L \frac{\partial}{\partial t} (f_s \rho). \tag{12}$$

Note that there is no diffusion-like or convection-like source term. It should, however, be mentioned that equation (12) is valid only for $\mathbf{V}_s = 0$.

In order to complete the formulation of the momentum equation, equation (2), the permeability tensor, $\mathbf{K}^{(2)}$, must be specified. Here, the principal flow directions of interdendritic liquid have been selected to be parallel and normal to the primary dendrite arms. If the dendrite growth direction is not changed throughout the entire domain and process as is in a unidirectional solidification system, it is relatively simple to deal with the anisotropic permeability. In general, however, the growth direction does not necessarily coincide with imposed thermal conditions or coordinate axes. Accordingly, an appropriate model which relates the components of the permeability to the dendrite growth direction is needed. In this study, the growth direction of the primary dendrite arms is assumed to be parallel to local instantaneous temperature gradients. Although it is not clear that the assumption is still valid in the presence of thermo-

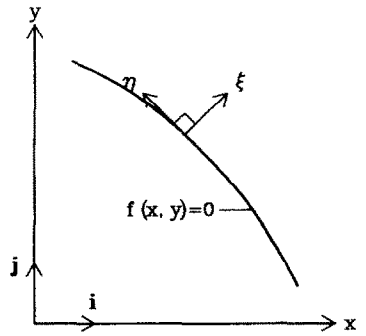

FIG. 1. Principal directions of the permeability tensor.

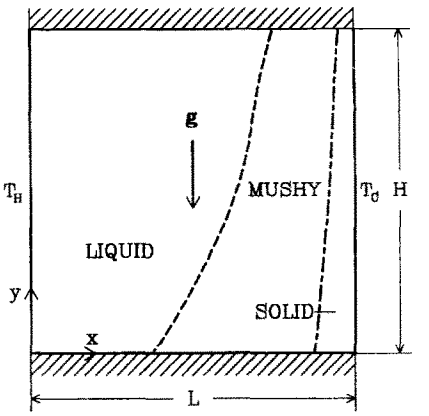

FIG. 2. Schematic of the physical model and coordinate system.

solutal convection, at least it is valid under constrained growth conditions where the heat and mass are transferred by diffusion only [19].

Let (ξ, η) be the directions normal and parallel to a local isotherm, $f(x, y) = 0$, at an arbitrary time as shown in Fig. 1. Then, (ξ, η) coincides with the principal axes of the permeability tensor $\mathbf{K}^{(2)}$. It is straightforward to express each component of $\mathbf{K}^{(2)}$ in terms of the principal values, K_ξ, K_η, and $f(x, y)$, that is,

$$\mathbf{K}^{(2)} = \left(\frac{1}{1+f'^2}\right)\begin{bmatrix} f'^2K_\xi + K_\eta & f'(K_\xi - K_\eta) \\ f'(K_\xi - K_\eta) & K_\xi + f'^2K_\eta \end{bmatrix} \tag{13}$$

where f' is a derivative of f with respect to x. Consequently, the Darcian damping term in equation (2) has the following specific form

$$\frac{\bar{\mu}\mathbf{V}}{\mathbf{K}^{(2)}} = \frac{\bar{\mu}}{(1+f'^2)}\begin{bmatrix} \left(\frac{f'^2}{K_\xi} + \frac{1}{K_\eta}\right)u + f'\left(\frac{1}{K_\xi} - \frac{1}{K_\eta}\right)v \\ f'\left(\frac{1}{K_\xi} - \frac{1}{K_\eta}\right)u + \left(\frac{f'^2}{K_\eta} + \frac{1}{K_\xi}\right)v \end{bmatrix}. \tag{14}$$

In the above expressions, the derivative f' should be determined at every location as a function of time. Also, note that the non-diagonal terms of $\mathbf{K}^{(2)}$ vanish in the case of the isotropic permeability or when the physical coordinates coincide with the principal axes.

The permeability tensor still involves unspecified principal components K_ξ and K_η. Unfortunately, the available experimental correlations [7] for these components cannot be applied beyond the limited range of the liquid volume fraction ($0.19 \leqslant g_l \leqslant 0.66$). In a typical solidification process of NH_4Cl–H_2O with an initial H_2O concentration of 0.7, the liquid volume fraction of the mushy region is always greater than 0.8 before eutectic solidification takes place. Moreover, since the permeability approaches infinity as the liquid volume fraction becomes close to unity, the permeability at large values of g_l is of particular importance. Accordingly, the permeability should be evaluated from a theoretical model which covers its limiting behavior. In the absence of a more appropriate permeability–porosity relation, the Blake–Kozeny model was adopted in this study,

$$K = K_0 \frac{g_l^3}{(1-g_l)^2} \tag{15}$$

where the coefficient K_0 is a function of the dendrite arm spacings. To accommodate this model in an anisotropic case, K in equation (15) is considered to be a representative permeability of the system which is the geometric mean of K_ξ and K_η,

$$K = (K_\xi K_\eta)^{1/2}. \tag{16}$$

The principal permeability ratio, R, is also introduced as a measure of the anisotropy. It is defined as a ratio of the permeability component parallel to the primary dendrite arms to that normal to them, i.e.

$$R = K_\xi / K_\eta. \tag{17}$$

The ratio R, of course, should be a function of the volume fraction and the dendrite arm spacings, but the functional relation is not available for large values of g_l, therefore, a parametric study is considered. Three constant values of R, 0.5, 1.0, and 2.0 have been selected based on the experimental study for intermediate range of g_l and representative dendrite arm spacings. In this way, we can examine the effects of the anisotropy while the permeability of the system is kept constant in an average sense.

The physical system simulated in this study is depicted in Fig. 2, which corresponds to a representative experimental test arrangement [8]. Initially, superheated NH_4Cl–H_2O solution of uniform H_2O concentration C_{in}, and at temperature T_H fills the cavity. From time $t \geqslant 0$, the temperature of the right wall is suddenly changed to T_c, which is chosen to be below the eutectic temperature T_e to show the model capability, while the left wall is kept at temperature T_H. Solidification is initiated at the cold wall, and thermosolutal convection develops with time. Since T_C is lower than T_e, there exist three distinct regions, i.e. pure solid, mushy, and pure liquid

Table 1. Data used in the present study

	Initial and boundary conditions	
L	Cavity dimension [m]	0.0476
C_{in}	Initial concentration	0.70
T_H	Initial and heated wall temperature [K]	307.5
T_C	Cooled wall temperature [K]	253.15

Thermophysical properties for NH_4Cl–H_2O system [11, 12, 20, 21]

	Solid	Liquid
Density [kg m^{-3}]	1077.73	1077.73
Specific heat [J g^{-1} K^{-1}]	1870	3249
Thermal conductivity [W m^{-1} K^{-1}]	2.7	0.468
Diffusivity [m^2 s^{-1}]	—	1.8×10^{-9}
Viscosity [kg m^{-1} s^{-1}]	—	1.3×10^{-3}
Latent heat of fusion [J kg^{-1}]	3.138×10^5	
Thermal expansion coefficient [K^{-1}]	3.8321×10^{-4}	
Solutal expansion coefficient	0.25679	
Eutectic temperature [K]	257.75	
Eutectic concentration	0.803	
Equilibrium partition coefficient	0	
Permeability coefficient K_0 [m^2]	5.556×10^{-12}	

regions. The solidification continues until the steady state is reached.

The dimensions of the system and the imposed solidification conditions are listed in Table 1. The thermophysical property data used in the computations were obtained from various sources [11, 12, 20, 21] and are summarized in Table 1. Although the model equations which have been described allow the density to vary with the phase, the density is assumed to be constant to ensure volume conservation as required by a fixed-grid numerical method. Impermeable walls as well as the constant density make the boundary conditions very simple,

$$u = v = 0, \quad T = T_H, \quad \frac{\partial C}{\partial x} = 0 \quad \text{at } x = 0 \tag{18}$$

$$u = v = 0, \quad T = T_C, \quad \frac{\partial C}{\partial x} = 0 \quad \text{at } x = L \tag{19}$$

$$u = v = 0, \quad \frac{\partial T}{\partial y} = 0, \quad \frac{\partial C}{\partial y} = 0 \quad \text{at } y = 0 \text{ and } L. \tag{20}$$

Method of solution

The model equations were discretized by the control-volume based finite difference method and were solved using the iterative SIMPLER algorithm [22]. Since the square cavity in which NH_4Cl–H_2O solution solidifies has been studied extensively, selection of an appropriate grid system is relatively easy. Various grids, e.g. 30×30 [15], 42×42 [23], and 50×50 [8] have been used to resolve the details of the flow structures in the liquid and the mushy regions for different imposed conditions. By examining these studies, it was established that the 50×50 grid is able to reveal the essential features of the transport process. The grid was slightly skewed in the x- and y-directions to provide a denser distribution of nodal points near the walls where the velocity, temperature, and concentration gradients need to be accurately resolved.

The preliminary computations showed that, for all simulated cases, a time increment of $\Delta t = 1$ s was sufficient to achieve convergence. Nevertheless, $\Delta t = 0.5$ and 0.75 s were used to ensure the convergence until 300 s of simulation time, i.e. at the early stage of the solidification where overall flow structures were changing rapidly. For each time step, the iterations were terminated when the residual source of mass was less than 1×10^{-8}. Actually, this convergence criterion is severe enough to guarantee the conservation of the solute and to ensure that all the dependent variables remain unchanged. In this manner, each 1 s of simulation time required 15–20 s of CPU time on a CDC Cyber 205 supercomputer using the 50×50 grid. Calculations for every simulation continued until $t = 2100$ s, when the solidification reached nearly the steady state in a numerical sense.

RESULTS AND DISCUSSIONS

Simulations performed and validations

Simulations were performed for three different values of the principal permeability ratio, i.e. $R = 0.5$, 1.0, and 2.0, for the same solidification conditions and with the same average permeability in order to restrict our focus on investigating the effects of the anisotropy. Plots for streamlines, isotherms, and liquid isocomposition-lines have the liquidus boundary superimposed as thick dotted lines. Streamlines associated with the clockwise rotating convection cells

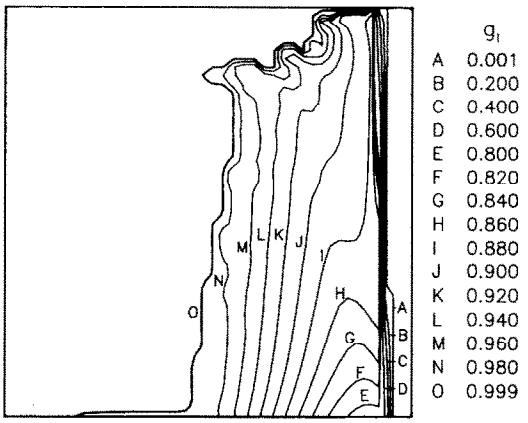

FIG. 3. Typical example of the liquid volume fraction distribution ($R = 1.0$, $t = 20$ min).

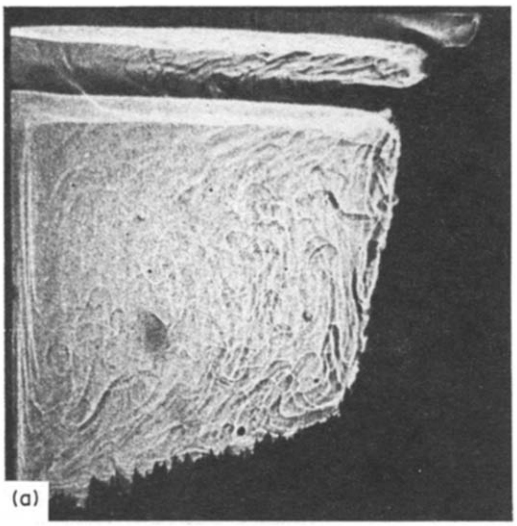

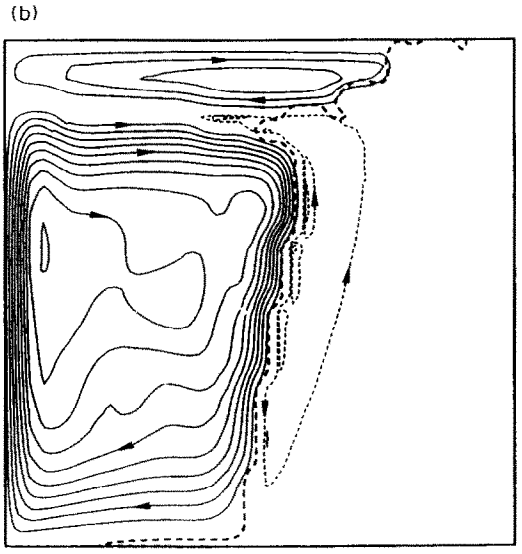

FIG. 4. Comparison of the double-diffusive layer formation at $t = 20$ min: (a) experimental [24] and (b) predicted.

(solid lines) have negative values, while dotted streamlines which are positive-valued denote counterclockwise rotating cells. All positive- and negative-valued streamlines were plotted in the prescribed increments of 1.5×10^{-4} and 7.5×10^{-4}, respectively, to show the flow intensity as well as the structure. Isotherms and liquid isocomposition contours are presented in ten equal increments of the normalized quantities, $(T-T_C)/(T_H-T_C)$ and $(C_l-C_{in})/(C_e-C_{in})$, respectively.

Prior to discussing the results of the simulations, the validity of the Blake–Kozeny model needs to be addressed. As shown in Fig. 3, the mushy region is very dilute, except in a very narrow region between lines A and E where eutectic solidification takes place. Since the Blake–Kozeny model is known to be applicable to small liquid volume fractions g_l, it seems inappropriate to use it in the present study. No experimental correlation which is valid for large g_ls is, however, available in the literature. Also, the anisotropic effects are not expected to be drastically changed when a more realistic model is used instead. Considering these facts, it is thought that Blake–Kozeny model is useful, at least, for a parametric study, if reasonable values for the parameters, i.e. the permeability ratios, are selected.

To validate the model predictions, a representative case has been compared with available experimental results. The lack of detailed experimental data for temperature and/or concentration distributions means that the comparison was made only for flow structure which shows the essential features of the transport phenomena during the solidification process. In Fig. 4, a predicted flow pattern for an isotropic case ($R = 1.0$) at $t = 20$ min is compared with a shadowgraph image which had been taken under the same conditions [24]. The comparison indicates that the present model is able to resolve the double-diffusive convection cells and the macroscopic solid–liquid interface (liquidus) morphology successfully. A significant difference, however, exists in the thickness of the mushy region formed along the bottom as well as the cooled wall which is directly related to the solidification rate. The disagreement in the liquidus position along the cooled wall has also been reported by Christenson and Incropera [10]. They attributed it to the weakness of model assumptions such as laminar flow, local thermodynamic equilibrium, isotropic permeability, and uncertainty of the properties. The same limitations are also true for this study, except that the isotropic permeability assumption has been relaxed and is to be examined. In addition to these reasons, thermal inertia effects of the cavity walls which have been completely neglected can also contribute to the difference. On the other hand, the mushy region formed along the adiabatic bottom

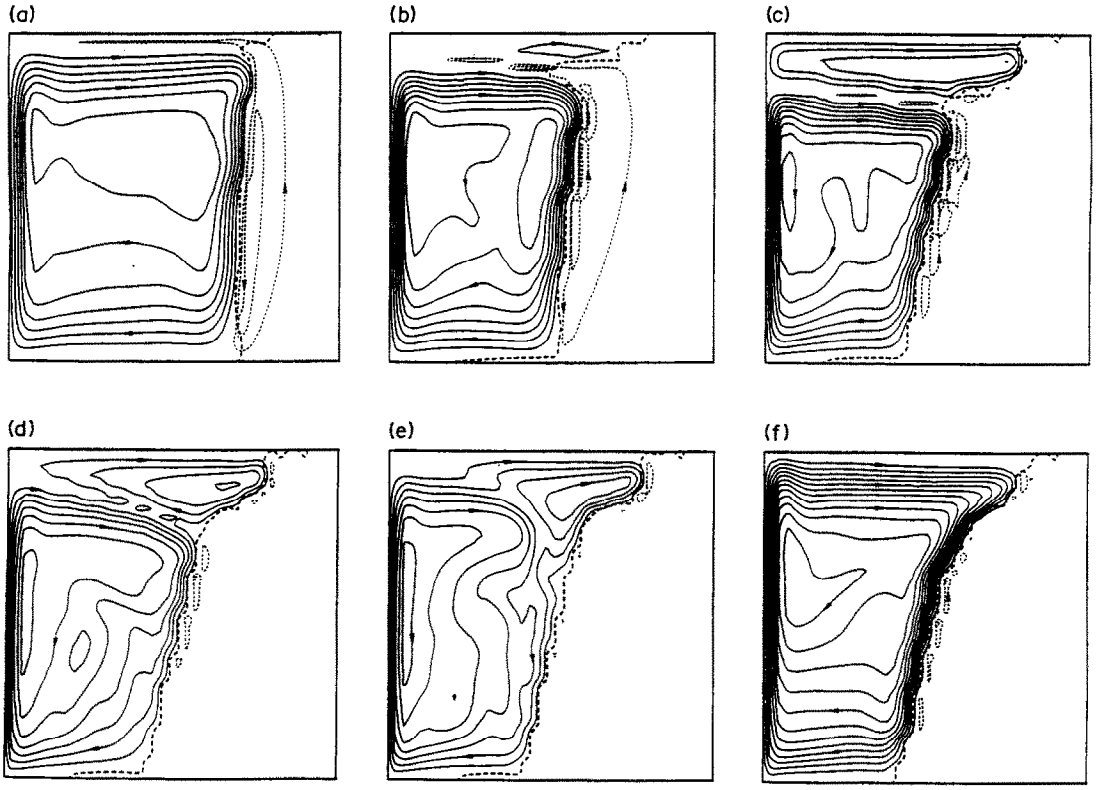

FIG. 5. Development process of the double-diffusive convection for the isotropic case: (a) $t = 5$ min, (b) $t = 15$ min, (c) $t = 25$ min, (d) $t = 30$ min, (e) $t = 30$ min 15 s, and (f) $t = 35$ min.

wall in the shadowgraph is the result of the floating and settling of detached dendrite arms during the initial stages of the solidification [8]. Since the mechanism of floating and settling is not understood, it is not modeled. Even though there are some quantitative discrepancies between the predicted and the experimental results, and the comparison is limited to the specific case, the model predictions show the qualitative agreement in the fundamental features and trends of the solidification process. The model can, therefore, be used to investigate the effects of the anisotropy.

Results for isotropic case

Since the nature of the fundamental transport phenomena is expected to be similar for all simulated cases, the time evolution of the solidification process for a representative case (naturally the isotropic case, $R = 1.0$) is described first, then, the focus is on the discussion of differences among three simulations, i.e. the anisotropic effect. Figure 5 illustrates the flow patterns for $R = 1.0$ at selected times. At the early stage of solidification (Fig. 5(a)), the water-rich liquid which resulted from the solubility differences between the solid and liquid phases in the mushy region moves upward by the solutal buoyancy force against the thermal buoyancy force and forms a thin liquid layer below the top wall. In the pure liquid region below the upper layer, clockwise rotating cell develops owing to the temperature difference between the heated wall and the liquidus front. Despite the low temperature of the thin upper layer, high water concentration prevents the uppermost part of the liquid from solidifying. Due to sustained flow of water-rich liquid from the mushy region to the upper layer, the vertical thickness of the layer grows with the progression of time, forming a double-diffusive interface which separates colder, water-rich liquid layer from the warmer, water-deficient liquid in the lower convection cell. When the upper layer reaches a certain thickness, the thermal buoyancy forces initiate a recirculating flow inside the layer (Fig. 5(b)). As a result of this convective motion, remelting takes along the liquidus adjacent to the upper layer.

With increasing time, the flow of interdendritic liquids into the upper layer is greatly diminished (compare the dotted lines in Fig. 5(c) with those of Fig. 5(a)), while remelting continues by the fully developed thermal convection in the upper layer. This produces a decrease in the H_2O concentration of the liquid. On the other hand, flow interaction (this will be discussed later in detail) between the lower layer and the mushy region increases the concentration of the liquid in the lower layer. The small concentration difference

between two layers, means that the thermal buoyancy forces in the lower layer become predominant over the density stratification forces which have maintained the double-diffusive interface, particularly in the vicinity of the heated wall where the recirculating flow is strongest, then, the double-diffusive interface tilts downward away from the heated wall and becomes unstable as shown in Figs. 5(d) and (e). The solidification and the remelting along the liquidus continues as the flow is changing, but the rate is very small. In the final stage, the interface breaks up so that a single thermal convection cell is established over the entire liquid region (Fig. 5(f)).

Effect of permeability ratio

Now, let us consider the influences of the principal permeability ratio, R, on the solidification process. Figures 6 to 8 correspond to $R = 0.5$, 1.0, and 2.0, respectively, and show streamlines, isotherms, and liquid isocomposition-lines at a representative time ($t = 20$ min). First of all, the vertical thickness of the upper layer which is clearly shown by the isocomposition-lines (Figs. 6(c), 7(c), and 8(c)) is increased with decreasing R. Differences are also found in the intensity of the recirculating flow in the upper layer, in the temperature and the concentration distributions. These are, in fact, of practical importance for the control of solidification processes. The differences have resulted from the interdendritic flow structures which are represented by the dotted lines in Figs. 6(a), 7(a), and 8(a). For convenience of the discussion, it is assumed that the principal directions of the permeability tensor coincide with the coordinate axes. Actually, this assumption is valid over most of the mushy region, because the temperature distributions (Figs. 6(b), 7(b), and 8(b)) are nearly parallel to the cooled wall, except the uppermost part of the region modeled. The permeability components in the vertical and horizontal directions are then simply K_η and K_ξ, respectively. From the definition of R, equation (17), K_η becomes large with decreasing R so that the upward interdendritic flow which is responsible for the upper layer growth is intensified. Since the driving force for the interdendritic flow which should be the solutal buoyancy force is acting in the vertical (gravitational) direction, K_ξ, despite increase according to R, hardly affects the flow structures in comparison with K_η.

Due to the nature of density stratification across the double-diffusive interface, the developing process of the double-diffusive cells can be illustrated by a concentration profile. In Fig. 9, time evolutions of the normalized liquid concentration vs the normalized height, y/L, at the middle of the cavity, $x/L = 0.5$, are presented for each simulated case. These profiles make it clear that the double-diffusive interface is characterized by a large concentration gradient across it. As solidification proceeds, the concentration of the upper layer decreases, while that of the lower layer increases. This fact provides background for the preceding discussions. With increasing R, the concentration as well as the depth of the upper layer decreases. The growth rate, of course, becomes smaller. Since the concentrations of the lower layers are nearly the same for all Rs at the same time, the mean liquid concentration over the entire liquid pool should be lower as R becomes larger. In other words, when R is large, the mushy region effectively retains much more water-rich liquid. The reason is the same as was discussed earlier; the smaller vertical permeability suppresses the interdendritic fluid flow. The mixture concentration, i.e. mass averaged concentration in the mushy region, should, therefore, be higher with increasing R.

This fact has been confirmed by Fig. 10, which shows the variation of the normalized average concentration, $(C - C_{in})/(C_e - C_{in})$, along the x-axis at the midheight of the cavity ($y/L = 0.5$) and at a certain time ($t = 20$ min). Approximately, the liquidus lies near the starting point of a sharp decrease (point A). The liquid region is at nearly uniform concentration, while the concentration in the mushy region varies with location. The curves for three values of R reveal similar trends, but are different in magnitude, par-

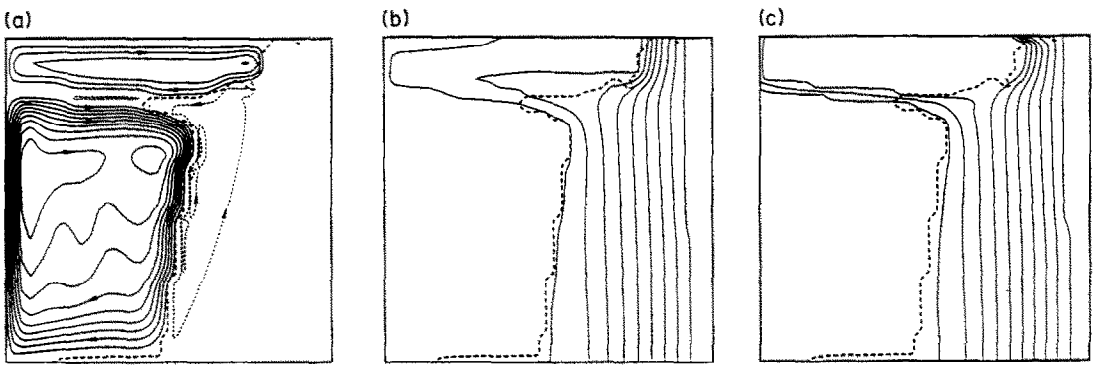

FIG. 6. Predicted results for $R = 0.5$ at 20 min: (a) streamlines, (b) isotherms (equal increments), and (c) liquid isocomposition-lines (equal increments).

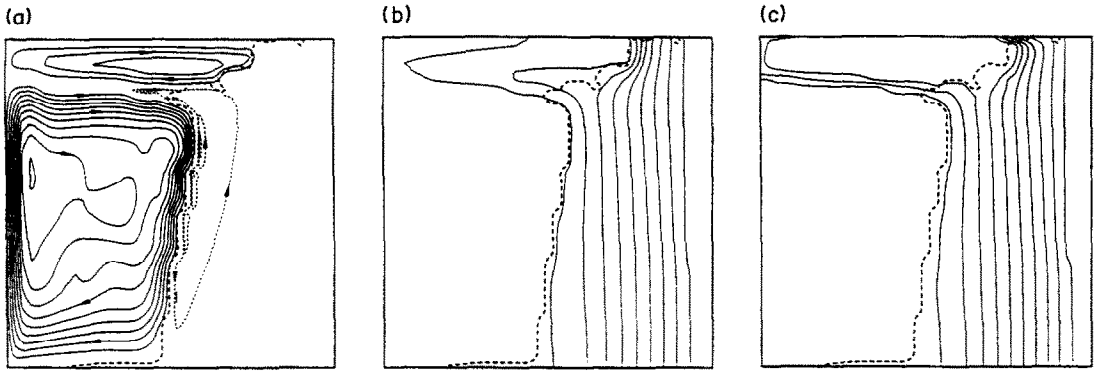

FIG. 7. Predicted results for $R = 1.0$ at 20 min: (a) streamlines, (b) isotherms (equal increments), and (c) liquid isocomposition-lines (equal increments).

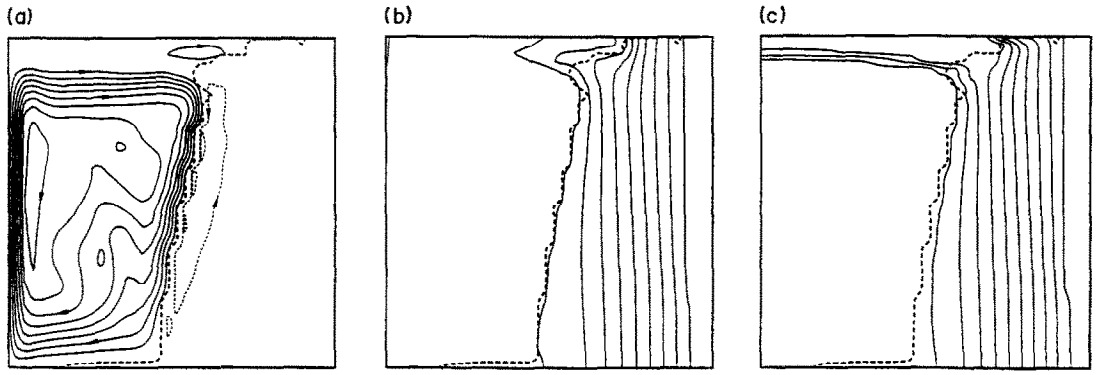

FIG. 8. Predicted results for $R = 0.2$ at 20 min: (a) streamlines, (b) isotherms (equal increments), and (c) liquid isocomposition-lines (equal increments).

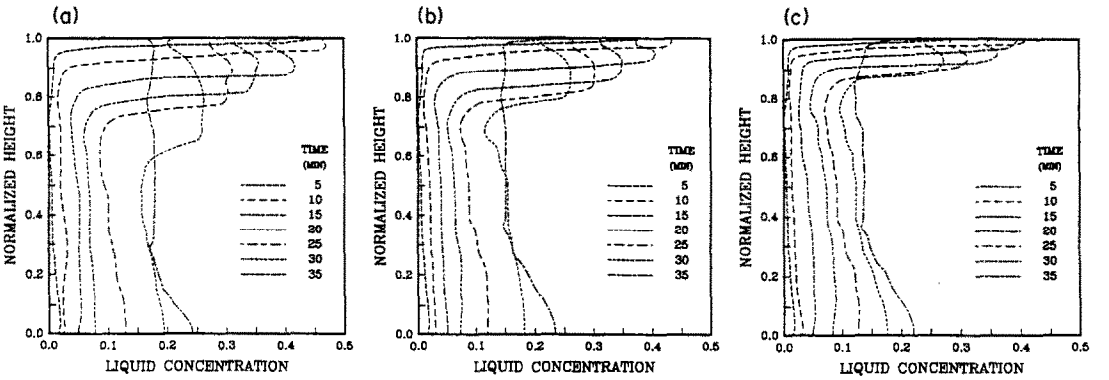

FIG. 9. Variation of the vertical liquid concentration profile with respect to time at $x/L = 0.5$: (a) $R = 0.5$, (b) $R = 1.0$, and (c) $R = 2.0$.

ticularly in the mushy region. Here, it is worth noting that the curves vary in decreasing, increasing, and again decreasing manner in the vicinity of the solidification front. This behavior indicates the flow interaction between the pure liquid and the mushy regions, as has been pointed out in the preceding discussion. The low mass diffusivity means that the species are transported mainly by the interdendritic flow in the mushy region near the liquidus. The penetration (or influence) depth of the flow is not, however, as large, because the permeability decreases sharply with decreasing liquid volume fraction (see

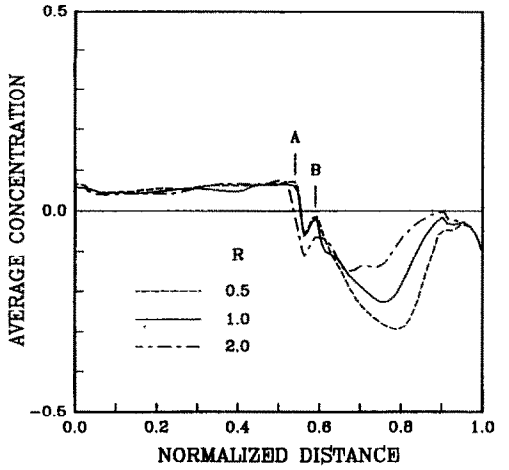

FIG. 10. Comparison of the horizontal concentration profiles at $y/L = 0.5$ and at $t = 20$ min.

equation (15)). The distance between the liquidus position (point A) and the local maximum point (point B) can be regarded as the penetration depth. Note that the depth for $R = 2.0$ is largest among the three cases considered. This is caused by the relatively large effective horizontal permeability K_ξ for $R = 2.0$. This type of concentration profile cannot appear in the problem with diffusion only. Further research is, however, needed to better understand the interaction of flow near the solidification front.

Time evolution of important physical quantities at a fixed location provide useful transient information on the transport process during solidification. Figure 11 depicts variations in the liquidus position, temperature, and liquid concentration with respect to time at three selected heights, $y/L = 0.133$, 0.5, and 0.867. These plots again reveal that complicated transport phenomena occur primarily in the upper portion of the system. It obviously resulted from the mutually opposing buoyancy forces in the present system. The situation is different when the thermal and the solutal buoyancy forces aid each other like in an aqueous sodium carbonate system [25]. It is, therefore, natural that the anisotropic effects appear at $y/L = 0.867$. Note that there is little difference between the simulated cases at $y/L = 0.133$ and 0.5.

Variations of the liquidus positions at $y/L = 0.867$ (Fig. 11(a)) indicate that a significant remelting is taking place along the solidification front. Although the temperature of the upper layer rises continuously beyond the local minimum (Fig. 11(b)), the decrease of the concentration (Fig. 11(c)) which makes the liquidus temperature higher results in no further remelting after a certain time. Here, the temperature and the concentration at $x/L = 0.5$ are considered as representative values at the height. The remelting is most severe when $R = 0.5$, not only because the earlier development of the thermal convection slows down the temperature decrease (near 15 min) in spite of the

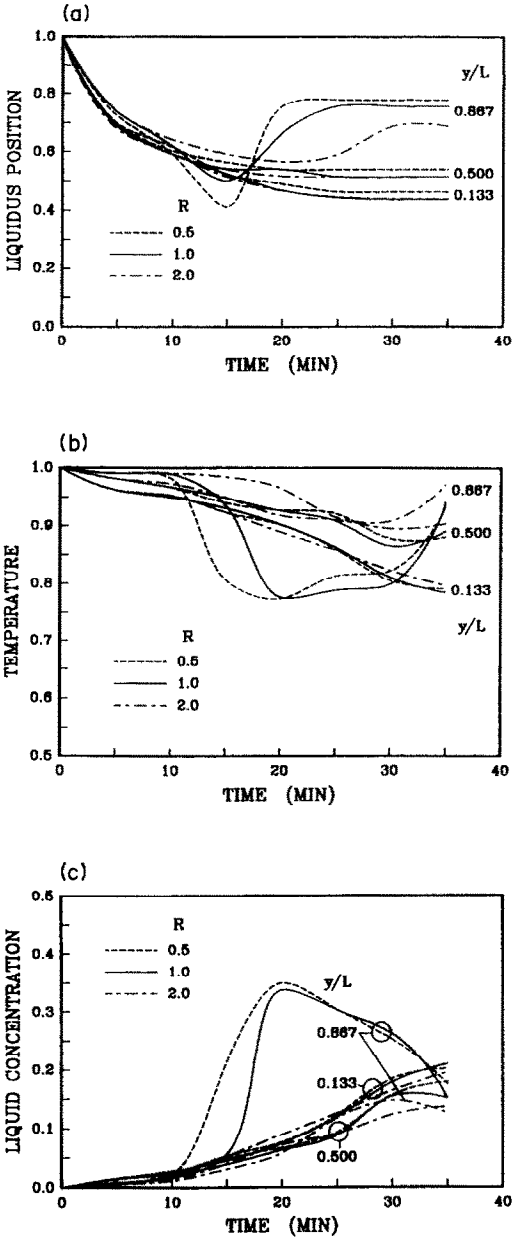

FIG. 11. Transient behaviors at different heights, $y/L = 0.133$, 0.5 and 0.867: (a) liquidus position, (b) temperatures at $x/L = 0.5$, and (c) liquid concentration at $x/L = 0.5$.

continuous supply of cold, water-rich liquid by the vigorous interdendritic flow, but also because the concentration at the beginning of the remelting period is already high enough to lower the liquidus temperature below the local temperature. The behavior of the temperature and the concentration at $y/L = 0.867$ can also be used to show the time evolution of the double-diffusive convection. The sharp decrease of the temperature means that the double-diffusive interface descends across the location. The slowdown of decrease and the increase of the temperature indicate

the development of the thermal convection in the upper layer. Due to a small concentration difference between the upper and lower layers at the later stage (Fig. 11(c)), the interface is broken up and the two layers merge into a single convection cell, which is shown by the uniform concentration and by the high temperature at $y/L = 0.867$. Since the upper layer for $R = 2.0$ is very thin, variations of the quantities at $y/L = 0.867$ appear as if the double-diffusive convection were absent. The differences in temperature and concentration at $y/L = 0.867$ are, however, large enough to show the anisotropic effects, that is, smaller R advances the cold, water-rich layer growth and thereby the onset of the thermal convection, also the final liquid concentration for $R = 0.5$ is greater than those for $R = 1.0$ and 2.0. It should be mentioned that the point ($x/L = 0.5$, $y/L = 0.133$) is in the mushy region at the final stage of solidification.

CONCLUSIONS

To investigate effects of an anisotropic permeability of the mushy region on the transport process during the solidification of binary mixtures, a numerical simulation of an aqueous ammonium chloride solution in a two-dimensional square cavity with heating/cooling vertical walls and adiabatic horizontal connecting walls has been conducted. A modified definition of the enthalpy allowed the energy equation to be expressed in the standard form without convection-like and diffusion-like source terms. A specific permeability tensor for which principal directions are parallel to and normal to the columnar–dendrite arms was derived in terms of the principal components and the local temperature gradient to incorporate the anisotropy in the momentum equations. The principal permeability ratio, R, which has been introduced as a measure of the anisotropy was assumed to be constant regardless of the liquid volume fraction. Simulations for three different values of R, 0.5, 1.0, and 2.0, were performed, while the mean permeability was kept fixed.

The computed results for a representative case agreed reasonably well with the available experimental observations in the sense that the essential features of the transport processes such as double-diffusive convection, macroscopic solid–liquid interface morphology, and remelting, were resolved successfully. The model capability was also shown by the predicted evolution of the solidification process, in which growth of the cold, water-rich layer, interdendritic flow structures, development of the secondary convection cell, remelting along the liquidus in the upper layer, break-up of the double-diffusive interface, and merging of two layers were revealed in detail.

The principal permeability ratios other than the unity correspond to anisotropic cases. Since the permeability basically controls the flow characteristics, effects of the anisotropy naturally appeared in the interdendritic flow structures. Smaller R which is equivalent to the larger effective permeability in the vertical direction resulted in the more vigorous interdendritic flow, which, in turn, promoted the growth of the upper layer and development of the thermal convection in the layer. The temperature and the concentration distributions were also changed because of their intimate coupling with the flow field. Owing to the strong flow in the mushy region, the concentration of the upper layer was higher with smaller Rs. Consequently, the concentration difference between the (partially) solidified and the pure liquid regions became larger with decreasing R, which is of particular importance in metallurgical applications. The depression of the liquidus temperature by the high concentration as well as the early developed thermal convection in the upper layer resulted in a severe remelting along the solidification front. The effective horizontal permeability, which is directly proportional to R, was found to be responsible for the flow interaction between the mushy and the pure liquid regions, although its contribution to the transport process is less significant than that of the vertical permeability.

Considering that the uncertainty involved in available permeability data is of the order of 10, the ratio of the principal value for the largest R to that for the smallest R treated in this study, e.g. $(K_\eta)_{R=0.5}/(K_\eta)_{R=2.0} = 2$, is very small. Nevertheless, the effects of the anisotropy on the transport process during solidification appeared to be very significant. The anisotropy in the permeability should, therefore, be taken into account in mathematical–numerical modeling of the process to obtain improved predictions.

Acknowledgements—This work was carried out when the first author (H.Y.) was on his sabbatical leave at Purdue University during the 1990–1991 academic year. He would like to express his appreciation to Gyeongsang National University, Chinju, Korea and Korea Science and Engineering Foundation for the financial support.

REFERENCES

1. R. A. Brown, Theory of transport processes in single crystal growth from the melt, *A.I.Ch.E. Jl* **34,** 881–911 (1988).
2. R. Viskanta, Mathematical modeling of transport processes during solidification of binary systems, *JSME Int. J., Series II* **33,** 409–423 (1990).
3. H. E. Huppert, The fluid mechanics of solidification, *J. Fluid Mech.* **212,** 209–240 (1990).
4. K. Murakami, A. Shiraishi and T. Okamoto, Fluid flow in interdendritic space in cubic alloys, *Acta Metall.* **32,** 1423–1428 (1984).
5. C. Y. Liu, K. Murakami and T. Okamoto, Permeability of dendrite network of cubic alloys, *Mater. Sci. Technol.* **5,** 1148–1152 (1989).
6. R. Nasser-Rafi, R. Deshmuhk and D. R. Poirier, Flow of interdendritic liquid and permeability in Pb–20 wt Pct Sn alloys, *Metall. Trans.* **16A,** 2263–2271 (1985).
7. D. R. Poirier, Permeability for flow interdendritic liquid in columnar–dendritic alloys, *Metall. Trans.* **18B,** 245–255 (1987).
8. C. Beckermann and R. Viskanta, Double-diffusive con-

vection during dendritic solidification of a binary mixture, *PhysicoChem. Hydrodyn.* **10,** 195–213 (1988).
9. D. G. Neilson, F. P. Incropera and W. D. Bennon, Numerical simulation of solidification in a horizontal cylindrical annulus charged with an aqueous salt solution, *Int. J. Heat Mass Transfer* **33,** 367–380 (1990).
10. M. S. Christenson and F. P. Incropera, Solidification of an aqueous ammonium chloride solution in a rectangular cavity—II. Comparison of predicted and measured results, *Int. J. Heat Mass Transfer* **32,** 69–79 (1989).
11. J. Szekely and A. S. Jassal, An experimental and analytical study of the solidification of a binary dendritic system, *Metall. Trans.* **9B,** 389–398 (1978).
12. S. Asai and I. Muchi, Theoretical analysis and model experiments on the formulation mechanism of channel-type segregation, *Trans. ISIJ* **18,** 90–98 (1978).
13. R. N. Hills, D. E. Loper and P. H. Roberts, A thermodynamically consistent model of a mushy zone, *Q. J. Mech. Appl. Math.* **36,** 505–539 (1983).
14. W. D. Bennon and F. P. Incropera, A continuum model for momentum, heat and species transport in binary solid–liquid phase change systems—I. Model formulation, *Int. J. Heat Mass Transfer* **30,** 2161–2170 (1987).
15. V. R. Voller, A. D. Brent and C. Prakash, The modelling of heat, mass and solute transport in solidification systems, *Int. J. Heat Mass Transfer* **32,** 1719–1731 (1989).
16. S. Ganesan and D. R. Poirier, Conservation of mass and momentum for the flow of interdendritic liquid during solidification, *Metall. Trans.* **21B,** 173–181 (1990).
17. W. D. Bennon and F. P. Incropera, Numerical analysis of binary solid–liquid phase change using a continuum model, *Numer. Heat Transfer* **13,** 277–296 (1988).
18. C. Prakash and V. R. Voller, On the numerical solution of continuum mixture model equations describing binary solid–liquid phase change, *Numer. Heat Transfer* **15,** 171–189 (1989).
19. W. Kurz and D. J. Fisher, *Fundamentals of Solidification*, Trans Tech Publications, Switzerland (1984).
20. *International Critical Tables and Numerical Data, Physics, Chemistry and Technology*, Vols. 3–4 (1928).
21. W. Bausch and W. Waidelich, On the thermal conductivity of ammonium- and deutero-ammonium chloride, *Phys. Lett.* **30A,** 190–191 (1969).
22. S. Patankar, *Numerical Heat Transfer and Fluid Flow*, Hemisphere, New York (1980).
23. A. H. H. Engel and F. P. Incropera, Solidification of a binary mixture in a square cavity with a free surface, *Wärme- und Stoffübertragung* **24,** 279–288 (1989).
24. C. Beckermann, Melting and solidification in binary systems with double-diffusive convection in the melt, PhD thesis, Purdue University, West Lafayette, Indiana (1987).
25. M. E. Thompson and J. Szekely, Mathematical and physical modelling of double-diffusive convection of aqueous solutions crystallizing at a vertical wall, *J. Fluid Mech.* **187,** 409–433 (1988).

EFFET DE L'ANISOTROPIE DE LA PERMEABILITE SUR LE TRANSPORT PENDANT LA SOLIDIFICATION D'UN MELANGE BINAIRE

Résumé—On simule numériquement la solidification d'un mélange binaire (NH_4Cl–H_2O) contenu dans une cavité carrée. La perméabilité anisotrope de la région boueuse est incorporée dans le modèle par un tenseur de perméabilité spécifique et le rapport R de perméabilité. La comparaison des résultats avec des données expérimentales connues montre que le modèle est capable de résoudre les caractéristiques fondamentales du mécanisme de solidification. Les effets de l'anisotropie paraissent être sensibles. Un petit rapport R de perméabilité aide à la croissance d'une couche secondaire mais aussi conduit à une grande différence de concentration entre la zone boueuse et celle de liquide pur. A cause de l'abaissement de la température du liquidus par une concentration élevée, et de la convection thermique développée plus tôt dans la couche supérieure, il se produit une fusion. De plus, l'intéraction d'écoulement à travers le front de solidification macroscopique devient plus importante quand le rapport R de perméabilité augmente.

DER EINFLUSS EINER ANISOTROPEN PERMEABILITÄT AUF DEN TRANSPORTPROZESS BEI DER ERSTARRUNG EINES ZWEISTOFFGEMISCHES

Zusammenfassung—Die Erstarrung eines in einem quadratischen Hohlraum enthaltenen Zweistoffgemisches (NH_4Cl–H_2O) wird numerisch untersucht. Die anisotrope Permeabilität des Verfestigungsgebietes wird mit Hilfe des spezifischen Permeabilitätstensors und des Permeabilitätsverhältnisses R in das Modell eingegliedert. Ein Vergleich der Ergebnisse mit früher berichteten Versuchsdaten zeigt, daß das Modell in der Lage ist, fundamentale Eigenschaften des Erstarrungsvorgangs zu beschreiben. Die Auswirkungen der Anisotropie scheinen dabei signifikant zu sein. Ein kleines Permeabilitätsverhältnis R fördert nicht nur das Wachstum der Sekundärschicht, sondern ergibt außerdem eine große Konzentrationsdifferenz zwischen dem Erstarrungsgebiet und der reinen Flüssigkeit. Es ergibt sich auch ein Wiederaufschmelzen aufgrund der konzentrationsbedingten Erniedrigung der Verflüssigungstemperatur und der bereits früher entwickelten thermischen Konvektion in der oberen Schicht. Zudem wird die Wechselwirkung der Flüssigkeit an der makroskopischen Erstarrungsfront mit wachsendem Permeabilitätsverhältnis R stärker.

ВЛИЯНИЕ АНИЗОТРОПНОЙ ПРОНИЦАЕМОСТИ НА ПРОЦЕСС ПЕРЕНОСА ПРИ ЗАТВЕРДЕВАНИИ БИНАРНОЙ СМЕСИ

Аннотация—Численно моделируется затвердевание бинарной смеси (NH_4Cl–H_2O), содержащейся в полости квадратного сечения. Анизотропная проницаемость двухфазной зоны учитывается специальным тензором проницаемости и отношением главных проницаемостей R. Сравнение результатов с ранее опубликованными экспериментальными данными показывает, что рассматриваемая модель позволяет определить основные особенности процесса затвердевания. Показано, что эффекты анизотропии являются существенными. Малое значение отношения проницаемостей R не только способствует росту вторичного слоя, но и приводит к большой разности концентраций двухфазной и жидкой областей. Кроме того, благодаря снижению температуры ликвидуса за счет большей концентрации и более раннего развития тепловой конвекции в верхнем слое происходит интенсивное вторичное плавление. Взаимодействие фаз через макроскопический фронт затвердевания усиливается с увеличением отношения проницаемостей R.